Engineering Structures 252 (2022) 113739

Contents lists available at ScienceDirect

Engineering Structures

journal homepage: www.elsevier.com/locate/engstruct

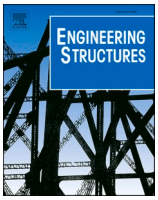

A new experimental-numerical approach to estimate peak wind loads on roof-mounted photovoltaic systems by incorporating inflow turbulence and dynamic effects

Johnny Estephan [a,*], Arindam Gan Chowdhury [a,b], Peter Irwin [b]

[a] Department of Civil and Environmental Engineering, Florida International University, Miami, FL, USA
[b] Extreme Events Institute of International Hurricane Research Center, Florida International University, Miami, FL, USA

ARTICLE INFO

Keywords:
Photovoltaic (PV) systems
Wall of wind
Large-scale testing
Partial Turbulence Simulation (PTS)
Aerodynamics
Dynamic response

ABSTRACT

Building appurtenances, such as rooftop photovoltaic (PV) systems, are vulnerable to damage during extreme wind events. To have more robust designs of PV systems, improved estimation of the peak wind effects is deemed necessary. The overall aim of this research is to develop a method for predicting peak wind loads on PV panels, including dynamic effects. For predicting peak pressures on roofs, the Partial Turbulence Simulation (PTS) method has been previously developed to allow for large-scale model testing by analytically incorporating the effects of the missing low-frequency turbulence based on the quasi-steady aerodynamic theory. The current paper focuses on a new experimental-numerical methodology by advancing the PTS approach to account for the dynamic amplification effects of rooftop PV systems. This is accomplished by mathematically applying a gust transfer function and a mechanical admittance function. The proposed advanced PTS approach is demonstrated using full- and small-scale wind tunnel testing of a PV panel mounted at different locations on the roof of a low-rise building with various tilt angles. The peak net force coefficients obtained from experimental testing of the PV panel were compared with those found in ASCE 7-16. Results showed that the ASCE 7-16 values, which currently do not take into consideration the wind-induced dynamic effects on rooftop PV systems, were significantly lower than the estimated peak force coefficients from the current study. This research describes a methodology for predicting peak wind loads on dynamically sensitive building appurtenances that can be used to inform wind load provisions in standards.

1. Introduction

The use of photovoltaic (PV) arrays as a source of renewable energy has become widely applied across the U.S. over the past few years. Currently, the U.S. is home to more than 2 million rooftop PV installations on commercial and residential buildings, and this number is expected to increase in the future [1]. Installed on the rooftop of low-rise buildings, PV panels are susceptible to damage under extreme wind events such as hurricanes. Such damage conditions could be aggravated should the peak wind loads acting on the supporting structures (including dynamic components) be underestimated.

A limited number of full-scale field studies have been undertaken to calibrate wind tunnel results [2–4]. Recently, in-situ measurements have been conducted on a rooftop PV array located on the Hogue Technology Center building at the Central Washington University (CWU) in Ellensburg, Washington [5,6]. Study findings showed higher net pressure coefficient values compared to those found in the ASCE 7-16 Standard [7]. Besides in-situ measurements, numerous experimental studies using large- and small-scale models have been undertaken in Boundary Layer Wind Tunnels (BLWTs) to investigate wind effects on rooftop PV panels [8–20]. Wind tunnel testing is a key experimental method for the evaluation of wind effects on rooftop PV panels of low-rise buildings and most findings were incorporated in the ASCE 7-16 Standard. However, new standards on rooftop PV systems are limited to simple geometries and orientations [5] and do not consider dynamic amplification effects [21,22]. Wind tunnel studies consisted of investigating the effects of several rooftop PV array parameters on wind-induced pressures. Such parameters included the array size, tilt angle, and panel's location on the roof. Wood et al. [17] carried out wind pressure tests on a 1:100 scale model of a large industrial building with solar panels mounted parallel to the flat roof. The authors found that the

* Corresponding author at: EC 3660, Florida International University Engineering Center, 10555 W Flagler St, Miami, FL 33174, USA.
E-mail address: jeste059@fiu.edu (J. Estephan).

https://doi.org/10.1016/j.engstruct.2021.113739
Received 8 March 2021; Received in revised form 23 November 2021; Accepted 5 December 2021

Nomenclature

Symbol	Description
$S_u(f)$	Wind speed spectral density
$S_{C_F}(f)$	Force coefficient spectral density
$S_{C_F}'(f)$	Response spectral density
B and R	Background and Resonance
$C_F(t)$	Force coefficient time history
$\overline{C}_F$	Mean force coefficient
$\widehat{C}_F$	Peak force coefficient
$\|\chi(f)\|^2$	Aerodynamic admittance function
$\|T(f)\|^2$	Gust transfer function
$\|H(f)\|^2$	Mechanical admittance function
m and p	Model and prototype
f	Wind forcing frequency
f_0	Natural frequency
ζ	Damping ratio
FS and PS	Full and partial spectra
b	PV panel width
L_p	PV panel length
h	PV panel height
$\overline{U}$	Mean wind speed
U_{3s}	3-sec gust speed
I_u	Turbulence intensity
${}^{x}L_u$	Integral length scale
A	PV panel area
g_B	Peak background factor
g_R	Peak resonance factor
$GC_{rn,nom}$	Nominal net pressure coefficient (ASCE 7-16)
GC_{rn}	Net pressure coefficient (ASCE 7-16)
γ_p	Parapet height factor
γ_C	Panel chord factor
γ_E	Array edge factor

panels' orientation with respect to the wind direction and their proximity to the leading edge significantly affect the pressure distribution. Kopp et al. [12] investigated the aerodynamic characteristics of a solar panel model consisting of six slender and parallel modules. The study findings showed that the highest wind loads were caused by vortex shedding from in-line panels. Kopp et al. [14] performed a series of wind tunnel experiments to evaluate the aerodynamic mechanisms associated with inclined solar panels mounted on flat roofs. It was found that array-generated turbulence increased wind loads for higher tilt angles, while the pressure equalization mechanism was more pronounced for lower tilt angles. Banks [8] conducted wind tunnel tests on tilted PV panels mounted on a flat roof of a low-rise building. The study highlighted the role of corner vortices in amplifying peak uplifts. Stathopoulos et al. [16] conducted an experimental investigation on the effects of rooftop PV panel location on the peak pressure coefficients. It was demonstrated that panels near roof edges experience the highest peak pressure coefficients.

Despite the major advancements in the experimental investigation of wind effects on PV panels, there are still major gaps in the fundamental knowledge that preclude the appropriate estimation of peak wind loads. Large-scale wind tunnel testing of low-rise buildings and their appurtenances provides the advantage of a more accurate modeling of the structural details and a better Reynolds number (Re) similarity with the prototype, as compared to small-scale testing [23]. However, owing to the limited sizes of typical BLWTs, large model scales render the low-frequency turbulence eddies largely unaccounted for in the simulation. To overcome this limitation, a Partial Turbulence Simulation (PTS) approach [21,24] has been previously developed at the NSF NHERI Wall of Wind (WOW) Experimental Facility (EF) [22,25] at Florida International University (FIU). The method consists of a post-test analysis to analytically incorporate the effects of the missing low-frequency turbulence in the peak pressure coefficients on rigid components, based on the quasi-steady aerodynamic theory. In addition to the PTS method, a hybrid method has been developed by Banks et al. [26] to analytically account for the effects of missing low-frequency turbulent energy on loads measured in the wind tunnel at large scales. The hybrid method consisted of a combination of analytical estimates and large-scale wind tunnel measurements to synthesize time series of wind loads that resemble full-scale measurements. Guo et al. [27] have developed a new method for estimating peak area-averaged pressure coefficients on the roof of a low-rise building model. The method is based on the quasi-steady vector model to account for the large-scale, low-frequency fluctuations of the upstream wind, and uses a stochastic model to account for small-scale and body generated turbulence effects. However, the partial turbulence simulation methods found in the literature apply only to rigid components and do not consider the dynamic resonant effects on flexible structures, such as PV panels. Dynamic effects have been investigated by previous studies on full- and small-scale rooftop PV panels [20,28,29] and other flexible structures (e.g., curtain wall systems [30]). The studies showed, based on field and full-scale wind tunnel measurements, that significant wind-induced vibrations may occur with natural frequencies as high as 14 Hz. Miller and Zimmerman [31] used pressure measurements to determine force coefficients on ground-mounted solar arrays and analyzed the dynamic response of the structure. In addition, Browne et al. [19] presented a method for determining the design wind loads for multi-row ground-mounted solar arrays, including both static and dynamic wind load coefficients. SEAOC PV2 [32] identified the need that solar array design shall consider vortex shedding and consequent dynamic resonant effects. These studies highlighted the well-established shortcomings of the ASCE 7-16 criterion for dynamically sensitive structures having a fundamental natural frequency ≤ 1 Hz, which was derived with whole buildings in mind and may well be misleading should it be applied to smaller structures (e.g., solar panels).

To fill these fundamental knowledge gaps, an improved methodology is needed to include low-frequency turbulence and wind-induced dynamic effects on building appurtenances. For this purpose, a new experimental-numerical method is proposed herein, and it consists of advancing the PTS method to consider dynamic effects. The proposed method requires a post-test analysis which consists of applying a gust transfer function to account for the missing low-frequency turbulence in large-scale testing. Moreover, resonant dynamic response effects of the PV panel are incorporated into the method by using the mechanical admittance function. The advanced PTS approach is illustrated using full- and small-scale wind tunnel testing of a rooftop PV panel. In the near future, the advanced PTS methodology will be validated by comparing the results from the experimental-numerical approach with those obtained from ongoing in-situ measurements on rooftop PV systems at CWU.

2. Background and theory

Based on the "quasi-steady" aerodynamic theory, low-frequency fluctuating forces or pressures on a structure (e.g. PV panels) are assumed to be proportional to the low-frequency longitudinal wind velocity fluctuations upstream [33]. The spectral density $S_{C_F(B)}(f)$ of the aerodynamic force coefficient on the PV panels is defined in Eq. (1).

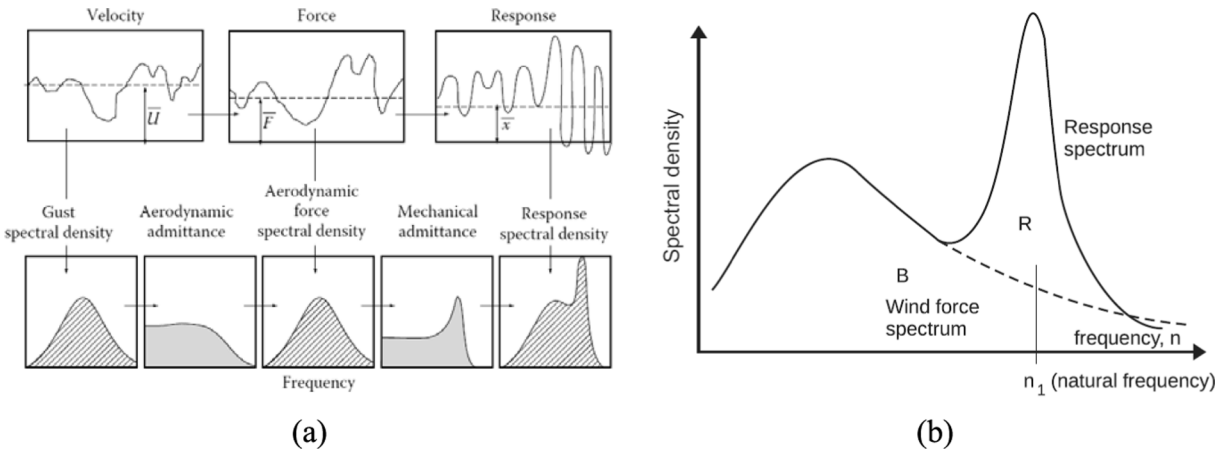

Fig. 1. (a) Wind loading chain; (b) Background and resonant components of the response spectrum [33] (Republished with permission of Taylor & Francis Group LLC - Books, from Wind Loading of Structures, John Holmes and Seifu Bekele, fourth edition, 2021; permission conveyed through Copyright Clearance Center, Inc.).

$$S_{C_F(B)}(f) = \frac{4\overline{C}_F^{\,2}}{\overline{U}^2}.|\chi(f)|^2.S_u(f) \tag{1}$$

where C_F is the net force coefficient on the PV panel, $|\chi(f)|^2$ is the aerodynamic admittance function, $\overline{C}_F$ is the mean aerodynamic force coefficient, $\overline{U}$ is the mean wind speed, and $S_u(f)$ is the power spectral density (PSD) of the longitudinal velocity fluctuations. It should be noted that subscript B stands for "background".

For small structures (e.g., PV panels) and at low frequencies, $|\chi(f)|^2$ shown in Fig. 1**a**, tends towards 1, whereas for high-frequency fluctuations, the effects of the aerodynamic admittance function are already captured in the experiments. For this purpose and based on the quasi-steady aerodynamic theory, Eq. (1) can be written in the form of Eq. (2):

$$S_{C_F(B)}(f) = \frac{4\overline{C}_F^{\,2}}{\overline{U}^2}.S_u(f) \tag{2}$$

The response spectral density, $S_{C_F(B+R)}'(f)$, which includes both the background (B) and resonant (R) components (Fig. 1**b**), can be calculated by applying a mechanical admittance function $|H(f)|^2$ (i.e., dynamic amplification function) to $S_{C_F(B)}$, as shown in Eq. (3).

$$S_{C_F(B+R)}'(f) = |H(f)|^2.S_{C_F(B)}(f) \tag{3}$$

where $|H(f)|^2$, shown in Eq. (4), is a function of the natural frequency of the structure (f_0), the forcing frequency (f), and the total damping ratio (ζ). The total damping ratio ζ is the sum of the aerodynamic (ζ_a) and structural (ζ_s) damping ratios.

$$|H(f)|^2 = \frac{1}{\left[1-\left(\frac{f}{f_0}\right)^2\right]^2 + 4\zeta^2\left(\frac{f}{f_0}\right)^2} \tag{4}$$

A full wind turbulence spectrum $S_{u,FS}(f)$ contains both the low- and high-frequency fluctuations, as is the case in the atmospheric boundary layer (ABL). A partial turbulence spectrum $S_{u,PS}(f)$, simulated during large-scale wind tunnel testing, closely matches the high-frequency portion of the fluctuations but fails to account for low-frequency components. A gust transfer function $|T(f)|^2$ can be used in the post-test analysis to incorporate the effects of the missing low-frequency turbulence [26]. This gust transfer function is determined based on the ratio of the full wind turbulence spectrum $S_{u,FS}(f)$ (i.e., Von-Karman spectrum) to the partial wind turbulence spectrum measured in the wind tunnel $S_{u,PS}(f)$, as shown in Eq. (5).

$$|T(f)|^2 = \frac{S_{u,FS}(f)}{S_{u,PS}(f)} = \frac{S_{C_F(B),FS}(f)}{S_{C_F(B),PS}(f)} \tag{5}$$

The full response spectrum $S_{C_F(B+R),FS}'(f)$, including the background and resonant response effects, can be obtained by mathematically applying mechanical admittance and gust transfer functions to the partial aerodynamic force coefficient spectrum $S_{C_F(B),PS}(f)$, as shown in Eq. (6). Note that the prime symbol (') is used in this paper to differentiate between aerodynamic and dynamic forces obtained from pressure and reaction force measurements, respectively.

$$S_{C_F(B+R),FS}'(f) = |H(f)|^2.|T(f)|^2.S_{C_F(B),PS}(f) \tag{6}$$

Except for *Re* effects, the peak pressure coefficients obtained using the original PTS approach for roof surface pressures were in general independent of wind speeds [21,24]. However, when resonant responses are present, the net force coefficients will vary with increasing wind speeds due to the dependence of the wind turbulence spectrum upon wind speed. In fact, increasing the assumed prototype mean wind speed ($\overline{U}_p$) suggests that the turbulent eddies at full scale are moving faster, causing a shift in the wind turbulence spectrum. Thus, for PV systems, the peak net force coefficients (including dynamic effects) need to be obtained as functions of prototype wind speeds. For codification purposes and ease of application by designers, the peak net force coefficients can be computed as a function of the reduced frequency $(f_0.b)/U_{3s}$, where b and U_{3s} represent the full-scale PV panel width and 3-sec gust speed, respectively. To obtain net force coefficient spectra at various prototype wind speeds, the mechanical admittance function can be presented as a function of assumed prototype mean wind speed ($\overline{U}_p$) and will be denoted by $\left|H\left(f_p\right)\right|^2$, as shown in Eq. (7). The mechanical admittance function of the prototype depends upon the forcing frequency f_p, which in turn depends upon the prototype wind speed. The dependence of f_p upon wind speed is expressed as $f_p = f_m\left(\frac{\lambda_L}{\lambda_U}\right)$. The frequency scale $\left(\lambda_f = \frac{f_m}{f_p} = \frac{\lambda_U}{\lambda_L}\right)$ can be obtained from the length scale $\left(\lambda_L = \frac{b_m}{b_p}\right)$ and velocity scale $\left(\lambda_U = \frac{\overline{U}_m}{\overline{U}_p}\right)$ which is based on the measured mean wind speed ($\overline{U}_m$) of the model and the assumed prototype mean wind speed ($\overline{U}_p$).

$$\left|H\left(f_p\right)\right|^2 = \frac{1}{\left[1-\left(\frac{f_p}{f_0}\right)^2\right]^2 + 4\zeta^2\left(\frac{f_p}{f_0}\right)^2} \tag{7}$$

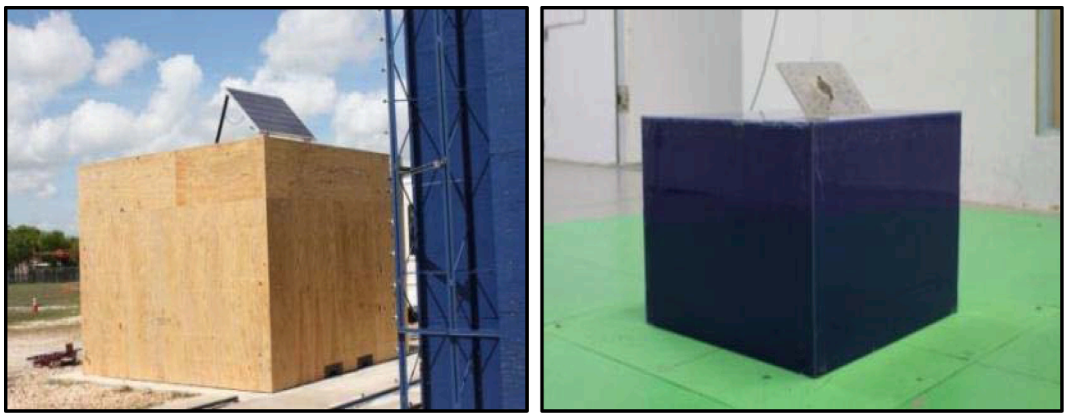

(a) Full-scale (1:1) model at WOW EF (b) Small-scale model (1:12) at BLWT of RWDI

Fig. 2. Test Specimens.

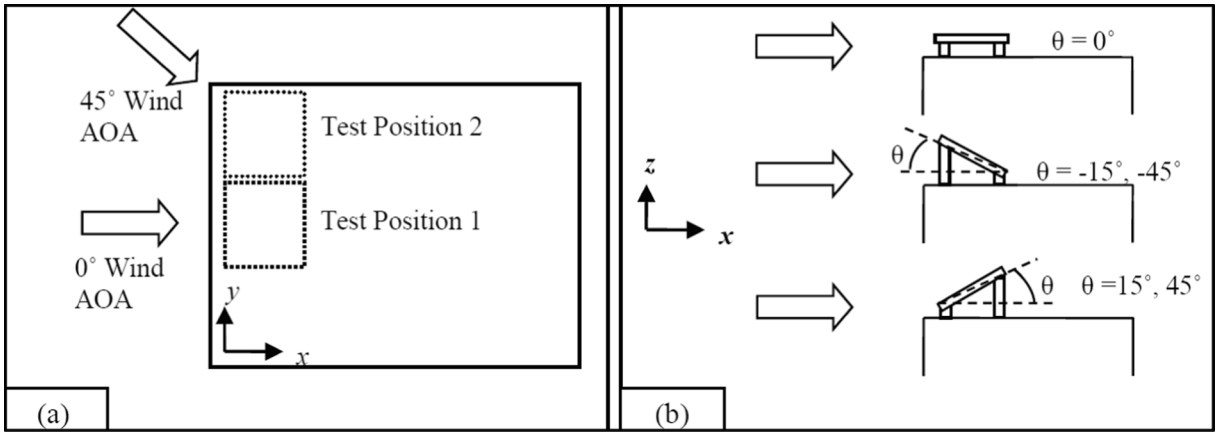

Fig. 3. Test plan: (a) wind directions and test positions, (b) PV tilt angles.

3. Methodology and experimental setup

3.1. Test specimens and instrumentation

To demonstrate the proposed advanced PTS approach, full-scale (1:1) experimental testing of a rooftop PV panel was performed using the 6-fan WOW facility, the predecessor of the NSF NHERI WOW EF at FIU; while small-scale model (1:12) experiments were performed at the boundary layer wind tunnel (BLWT) of RWDI USA LLC, respectively. The described specimens have the following full-scale dimensions: PV panel length L_p of 0.9 m (3 ft), panel width b of 1.6 m (5.2 ft), and a building height h of 3.5 m (11.5 ft) (see Fig. 2).

The full-scale model was instrumented with four multi-axial load cells mounted on the PV system's supports to collect net forces for a 3 min duration at a sampling frequency F_s of 100 Hz. For the small-scale model, a total of 28 pressure taps were installed on the upper and lower surfaces of the PV panel. Pressure taps consisted of polyurethane tubes connected to a Scanivalve data acquisition system to collect net pressure data for a duration of 90 s at a sampling frequency F_s of 512 Hz. A tubing transfer function was used to correct the collected pressure data for distortion effects introduced by the tubing length [34]. A low-pass filter function with a cut-off frequency of 100 Hz was applied to the collected pressure data. Detailed information on the experimental testing can be found in Moravej et al. [20].

Table 1
Testing protocol.

Case #	Position #	Full-scale $\overline{U}$ in m/s (mph)	Wind direction deg)	Panel tilt angle (deg)
1	1	25 (56)	0	0, −15, −45, 15, 45
2	2	25 (56)	0	0, −15, −45, 15, 45
3	2	25 (56)	45	0, −15, −45, 15, 45

3.2. Testing protocol

The full-scale specimen was tested at a mean wind speed $\overline{U}_m$ of 25 m/s (56 mph), obtained at a mean roof height h of 3.5 m (11.5 ft). The small-scale model was tested at a mean wind speed $\overline{U}_m$ of 8 m/s (18 mph), obtained at a mean roof height h of 0.3 m (1 ft). The model specimens were placed on the wind tunnel turntables and tested for different wind directions, test positions, and PV panel tilt angles (Fig. 3). The different test cases considered for experimental testing are summarized in Table 1. It should be noted that test position 1 refers to the location of the PV panel near the roof leading edge, while test position 2 indicates that the PV panel's location is at the roof corner. Also, a negative tilt angle indicates that the wind flow is acting towards the bottom surface of the PV panel, while a positive tilt angle designates that wind flow is acting towards the panel's top surface.

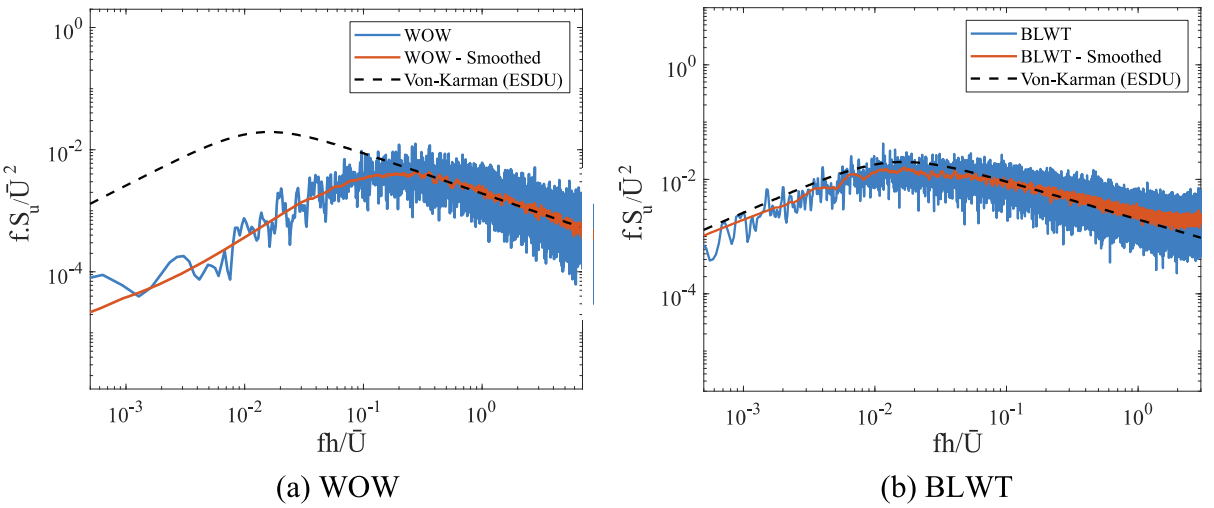

Fig. 4. Normalized PSD of the longitudinal velocity fluctuations.

Table 2
Test conditions for the prototype and WOW model.

Parameter	Unit	Prototype (Full-scale)	WOW Model
Turbulence intensity	%	$I_{up} = 19$	$I_{um} = 7$
Missing low-frequency turbulence	%	–	$I_{uL} = \sqrt{I_{up}^2 - I_{um}^2} = 18$
Integral length scale	m	${}^{x}L_{up} = 37$	${}^{x}L_{up} = 0.5$
PV panel length	m	$l_p = 0.9$	$l_m = 0.9$
Mean wind speed	m/s	$\overline{U}_p = 25$	$\overline{U}_m = 25$

3.3. Wind flow characteristics

As discussed in Section 1, full- or large-scale wind tunnel testing of low-rise buildings and appurtenances provides the benefits of accurately modeling the building and panel details while testing at a high Reynolds number (Re) to better capture the wind flow characteristics in nature. However, one challenge that the large-scale wind tunnel testing encounters is the missing low-frequency turbulence eddies in the simulated flow due to the size limitations imposed by the wind tunnel test section. Fig. 4 shows the simulated power spectral density (PSD) of the WOW and BLWT longitudinal velocity fluctuations corresponding to open terrain exposure ($z_0 = 0.02m$). Compared with the Von-Karman spectrum based on ESDU item 85020 [35], the WOW PSD shows a good match at the high-frequency portion of the fluctuations ($fh/\overline{U} > 0.1$) but lacks the low-frequency component. Contrary to WOW PSD, the BLWT simulates the entire turbulence spectrum as in natural wind including its low-frequency component.

The PTS approach, developed by researchers at the WOW EF at FIU, is based on the quasi-steady aerodynamic theory to correct the peak pressure coefficients for the missing low-frequency turbulence. The accuracy of the PTS method was previously validated in Mooneghi et al. [24] and Moravej [21] by comparing the PTS-corrected peak pressure coefficients that were obtained in the WOW with the field measurements of Silsoe cube [36] and Texas Tech University (TTU) building [37,38]. An approximate requirement for the quasi-steady assumption to be valid was derived by Mooneghi et al. [24] and was for $\frac{{}^{x}L_{um}}{b_m}$ to be greater than about 0.7, where ${}^{x}L_{um}$ is the longitudinal integral scale of the turbulence and b_m is the building dimension. In the PTS study, $\frac{{}^{x}L_{um}}{b_m}$ was calculated as 0.4 and 0.7 for the Silsoe cube and TTU building, respectively. Consequently, the experiments appeared to be on the borderline of applicability of the quasi-steady assumption. However, the results of the PTS method were well comparable with the full-scale peak pressure coefficients (obtained from field measurements). This indicates that even if the 0.7 criterion is not strictly achieved, acceptable results can still be obtained. In this study, while taking the PV panel length l_m as the relevant dimension, $\frac{{}^{x}L_{um}}{b_m}$ was calculated as 0.6 and the peak full-scale 3-sec gust speed U_{3s} was 40 m/s (90 mph). Table 2 summarizes the different test conditions for the prototype and WOW model.

The original PTS approach does not compensate for the wind-induced dynamic effects. Hence, an advancement of the PTS approach is proposed in this study to analytically incorporate not only the missing low-frequency turbulence effects but also the wind-induced dynamic effects.

3.4. Description of the advanced PTS approach

Net wind-induced reaction force and aerodynamic pressure data, collected from WOW and BLWT measurements respectively, were used to demonstrate the proposed advanced PTS approach. The net force coefficient time histories $C_F(t)$ for WOW and BLWT models are defined in Eqs. (8) and (9) as:

$$C_{F,WOW}{}'(t) = \frac{\sum_{i=1}^{4} F_i{}'(t)}{\frac{1}{2}\rho \overline{U}_m{}^2 . A} \tag{8}$$

$$C_{F,BLWT}(t) = \frac{\sum_{i=1}^{14} P_i(t) . A_i}{\frac{1}{2}\rho \overline{U}_m{}^2 . A} \tag{9}$$

In Eq. (8), $F_i{}'(t)$ is the time history of the net reaction forces measured by the i^{th} load cell and acting along the axis normal to the PV panel in N (lbs.), ρ is the air density in kg/m^3 (slugs/ft^3), $\overline{U}_m$ is the mean wind speed at the mean roof height of the model in m/s (mph), and A is the projected area of the PV panel normal to the applied force in m^2 (ft^2). In Eq. (9), $P_i(t)$ is the time history of the net aerodynamic pressure measured by the i^{th} tap, and A_i is the projected PV panel tributary area for the i^{th} tap in m^2 (ft^2).

Full-scale tests of the PV panel at WOW lack the low-frequency fluctuations but include the resonant component; whereas the BLWT tests simulate the entire turbulence spectrum as in natural wind but do not consider resonant effects due to the use of small-scale rigid models. The gust transfer function $|T(f)|^2$, discussed in Section 2, was used to incorporate the effects of missing low-frequency turbulence in the partial turbulence simulation when testing the full-scale model at WOW. Also, the mechanical admittance function $|H(f)|^2$ was used to compensate for the dynamic resonant effects in the case where rigid small-scale

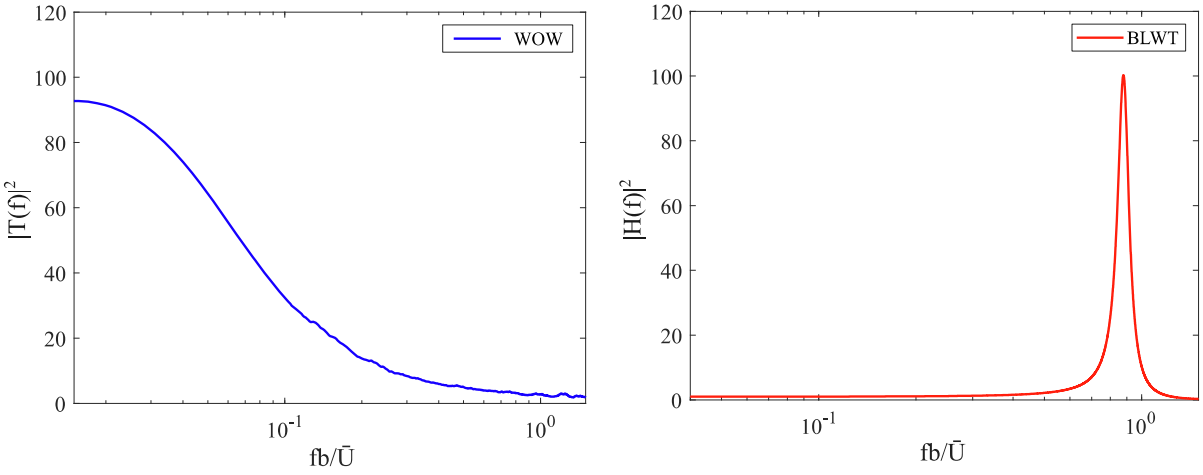

(a) Gust transfer function $|T(f)|^2$ (b) Mechanical admittance function $|H(f)|^2$

Fig. 5. Compensation functions.

models were tested at RWDI BLWT. The dynamic properties of the PV system used in the full-scale WOW testing (i.e., natural frequency f_0 and damping ratio ζ) were determined by applying the Random Decrement (RD) technique [39,40] to the net reaction forces measured by the load cells, which include the resonant response. The RD technique uses a time-domain approach in which the structural responses to operational loads of a certain structure are transformed into random decrement functions. The dynamic properties obtained using the RD technique ($f_0 = 14$ Hz and $\zeta = 5\%$) will serve as input parameters to $|H(f)|^2$.

Based on the proposed advanced PTS approach, the WOW response spectrum is compensated for missing low-frequency turbulence using $|T(f)|^2$, and that of BLWT is obtained by applying $|H(f)|^2$ to the net force coefficient spectrum. In the time domain, the compensated response time history $C_{F(B+R),FS}'(t)$ can be obtained using the Inverse Fast Fourier Transform (IFFT) which requires both the magnitude and phase information of the spectrum. However, since the phase information is not usually included in a power spectrum, the Fast Fourier Transform (FFT) [41] was first applied to the uncompensated net force coefficient data $C_F(n)$ to obtain the complex Fourier spectrum $z(k)$, as shown in Eq. (10).

$$z(k) = \sum_{n=1}^{N} C_F(n) e^{-2\pi i k n/N} \tag{10}$$

where k is the k^{th} term in the Fourier series, and n is the is n^{th} data point (ranging from 1 to N).

To obtain a compensated Fourier spectrum $z'(k)$, a complex gust transfer function $T(k)$ and mechanical admittance function $H(k)$, shown in Eq. (11), should be used with $z(k)$ instead of $|T(f)|^2$ and $|H(f)|^2$ since they include the real and imaginary parts.

$$H(k) = \frac{1}{\left(1 - \left(\frac{kf}{f_0}\right)^2\right)^2 + 4\zeta^2\left(\frac{kf}{f_0}\right)^2}\left(1 - \left(\frac{kf}{f_0}\right)^2 + 2\zeta\frac{kf}{f_0}i\right) \tag{11}$$

The compensated Fourier spectra of WOW and BLWT, including both the background and resonant components, can be calculated as $z'_{WOW}(k) = z_{WOW}(k).T(k)$ and $z'_{BLWT}(k) = z_{BLWT}(k).H(k)$. Using the IFFT approach, $C_{F(B+R),FS}'(t)$ can be computed from $z'(k)$, as shown in Eq. (12).

$$C_{F(B+R),FS}'(t) = \frac{1}{N}\sum_{k=1}^{N} z'(k) e^{2\pi i k n/N} \tag{12}$$

Peak net force coefficients $\widehat{C}_{F,FS-3s}$, normalized by 3-sec (full-scale) dynamic pressure, were estimated for 1-hr (full-scale) storm duration using extreme value analysis Type I based on Lieblein's best linear unbiased estimation (BLUE) method [42] with a 78% probability of non-exceedance and 100 subintervals.

Besides obtaining $\widehat{C}_{F,FS-3s}$ in the time domain, a simplified method was used to calculate $\widehat{C}_{F,FS-3s}$ in the frequency domain using the compensated spectra, as shown in Eqs. (13) through (16).

$$\widehat{C}_{F,FS-3s} = \overline{C}_{F,FS} + \sqrt{g_B^2 B + g_R^2 R} \tag{13}$$

$$g_R = \sqrt{2ln(\upsilon_R T)} + \frac{0.577}{\sqrt{2ln(\upsilon_R T)}} \tag{14}$$

$$B = \int_0^a S_{C_F(B),FS}(f)df \tag{15}$$

$$R = \int_0^a S_{C_F(B+R),FS}'(f)df - B \tag{16}$$

In Eq. (13), the background peak factor is $g_B = 3.4$ (g_Q in ASCE-7). In Eq. (14), υ_R can be conservatively taken as the natural frequency of the structure f_0, and T is the storm duration of 3600 sec. B and R, shown in Eqs. (15) and (16), are the background and resonant components of the net force coefficient spectrum, respectively. Peak net force coefficients were then obtained using time and frequency domain approaches as a function of the reduced frequency $(f_0.b)/U_{3s}$, where U_{3s} is used in the reduced frequency for codification purposes and ease of application by designers. It should be noted that the variation of the aerodynamic damping ζ_a as a function of wind speed was not investigated in this study, and a total damping of $\zeta = 5\%$ was used in the mechanical admittance function for all assumed prototype mean wind speeds.

4. Results and discussion

The proposed advanced PTS approach is illustrated by comparing the peak net force coefficients on the full-scale (WOW) model with those on the small-scale (BLWT) model. Then, the obtained peak net force coefficients on the WOW and BLWT models, including low-frequency turbulence and dynamic effects, were compared with those found in ASCE 7-16 for rooftop PV panels.

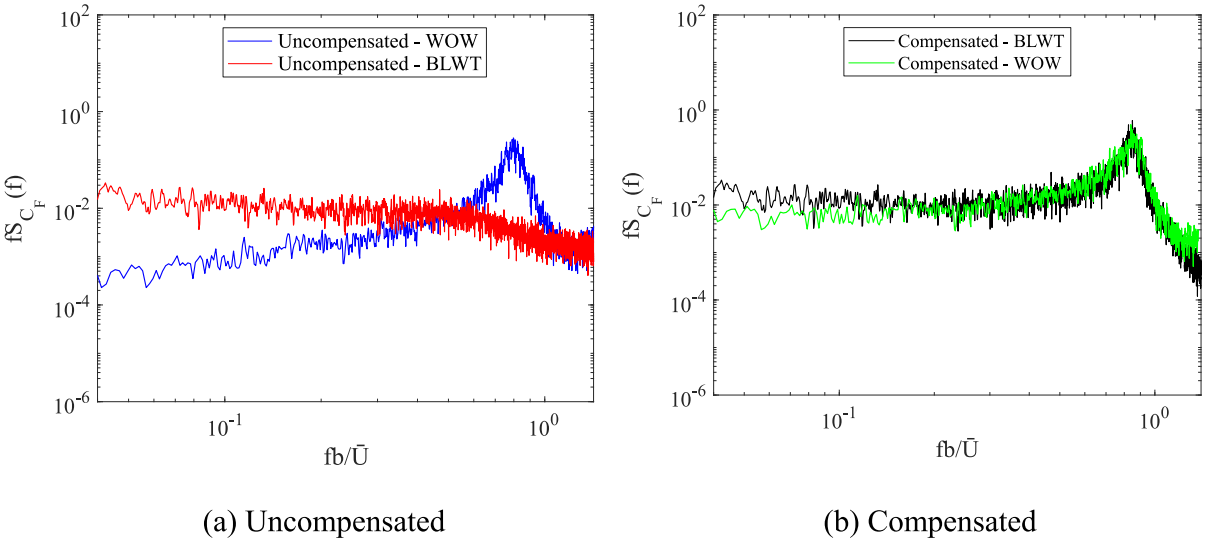

Fig. 6. Net force coefficient spectra for test case 3 and 0° PV tilt angle.

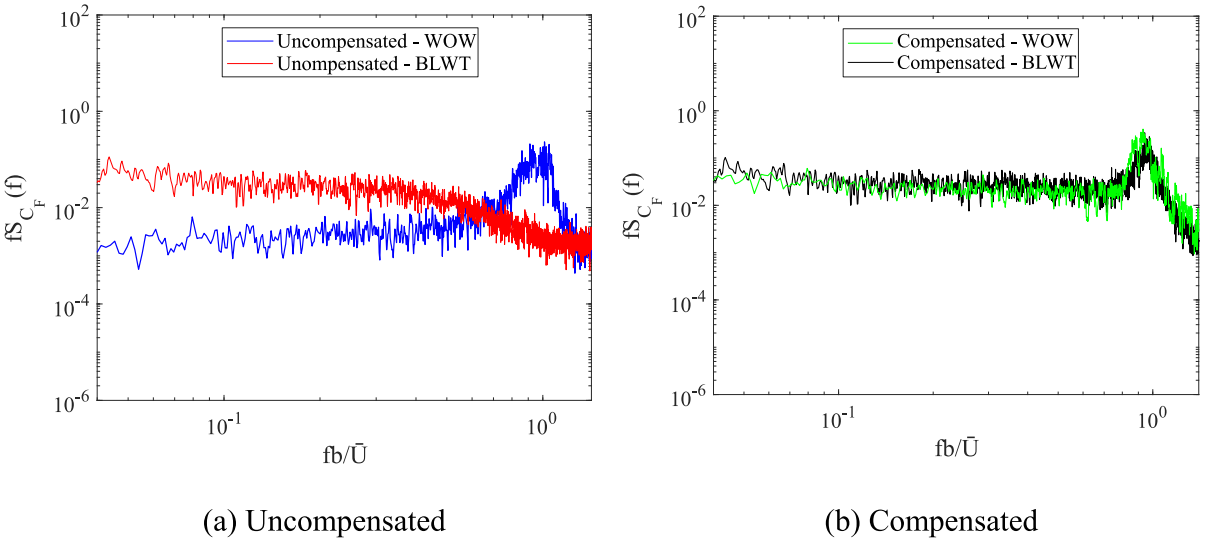

Fig. 7. Net force coefficient spectra for test case 3 and −45° PV tilt angle.

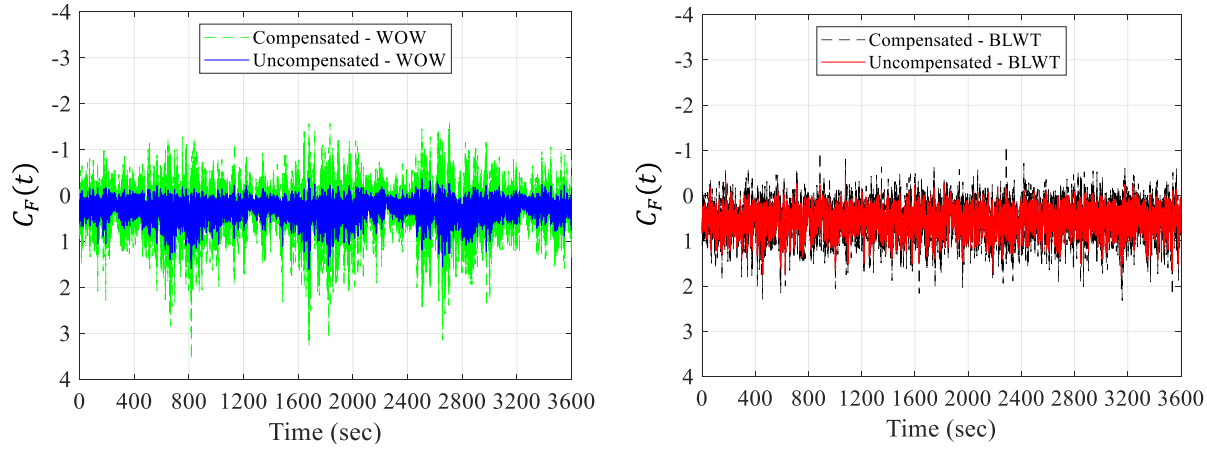

Fig. 8. Net force coefficient time history for test case 3 and 0° PV tilt angle.

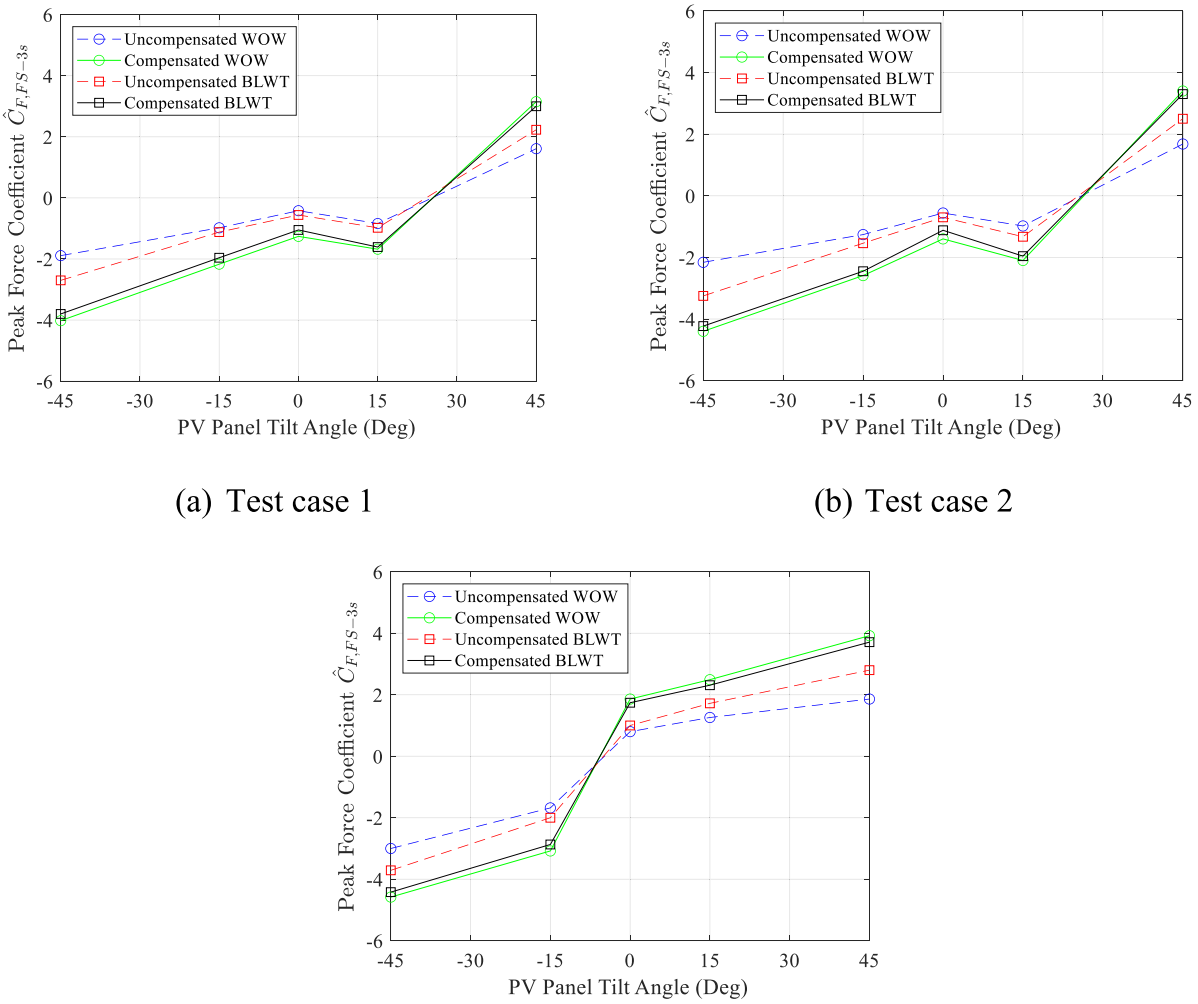

Fig. 9. Peak net force coefficients.

4.1. Compensated peak net force coefficients

The two compensation functions $|T(f)|^2$ and $|H(f)|^2$, described in Section 2, are illustrated in Fig. 5. $|T(f)|^2$ was used to incorporate the effects of low-frequency background fluctuations in the WOW net force coefficient spectra. It can be seen that a higher degree of PTS compensation is needed at low frequencies, whereas minimal to no compensation is needed at the high-frequency range. This further indicates that the PSD of the WOW longitudinal velocity fluctuations lacks its low-frequency component, while the high-frequency fluctuations are fully simulated. For the BLWT net force coefficients, the spectra were compensated by incorporating the dynamic resonant effects using $|H(f)|^2$, where the natural frequency of the primary mode of vibration (out-of-plane vibration normal to wind flow) and damping ratio of the PV system at full-scale were $f_0 = 14$ Hz and $\zeta = 5\%$, respectively.

Fig. 6**a and** 7**a** show the uncompensated net force coefficient spectra for test case 3 with 0° and −45° tilt angles, respectively. It can be seen that the WOW full-scale uncompensated net force coefficient spectrum is missing the effect of low-frequency background fluctuations while capturing the resonant effects. The uncompensated BLWT spectrum simulates the entire turbulence spectrum but does not capture resonant effects. Fig. 6**b and 7b** show the compensated WOW and BLWT net force coefficient spectra for test case 3 with 0° and −45° tilt angles, respectively. A reasonable agreement can be seen between the two compensated spectra, which include the effects of the background and resonant components of the response.

Fig. 8 shows the uncompensated and compensated $C_F(t)$ for WOW and BLWT. Fig. 9 shows $\widehat{C}_{F,FS-3s}$ for the various tilt angles and test cases being considered.

It is evident in Fig. 9 that both (1) full-scale system-level test results (WOW) without the incorporation of missing low-frequency turbulence effects, and (2) rigid scale model test results (BLWT) without the incorporation of dynamic effects, significantly underestimate the peak force coefficients $\widehat{C}_{F,FS-3s}$. The compensated $\widehat{C}_{F,FS-3s}$ of WOW and BLWT showed a reasonable agreement for all PV tilt angles, and the values were the highest for test case 3 and −45° PV tilt angle ($\widehat{C}_{F,FS-3s} = -4.5$). This can be attributed to the formation of conical vortices near the roof corner where negative net force coefficients (i.e., suction) are more pronounced [43]. It should be noted that $\widehat{C}_{F,FS-3s}$ values are slightly higher for the WOW model than for the BLWT. This can be partially attributed to the Reynolds number effects ($Re = 2.5 \times 10^6$ and 4.9×10^4 for the WOW and BLWT tests, respectively); however, further research is needed to investigate this aspect. The reference geometry considered for Re calculation is the PV panel width b. Also, the increase in tilt angle showed an increase in the estimated $\widehat{C}_{F,FS-3s}$ for all test cases. These observations are in line with the findings of Kopp [13] in which it was shown from wind tunnel data that increasing the overall height above

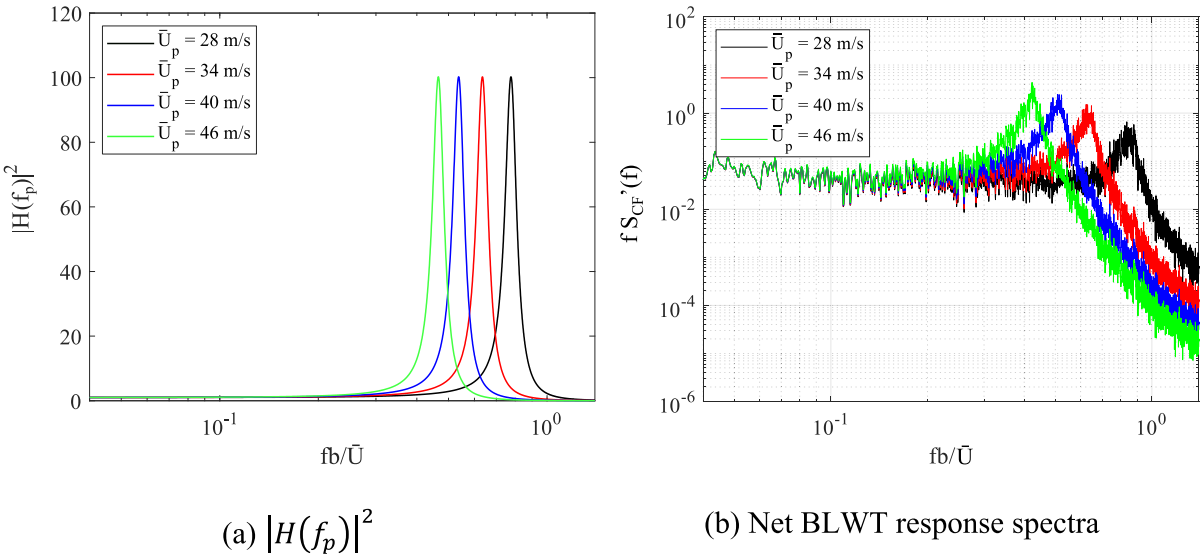

Fig. 10. Test case 3 and −45° PV tilt angle.

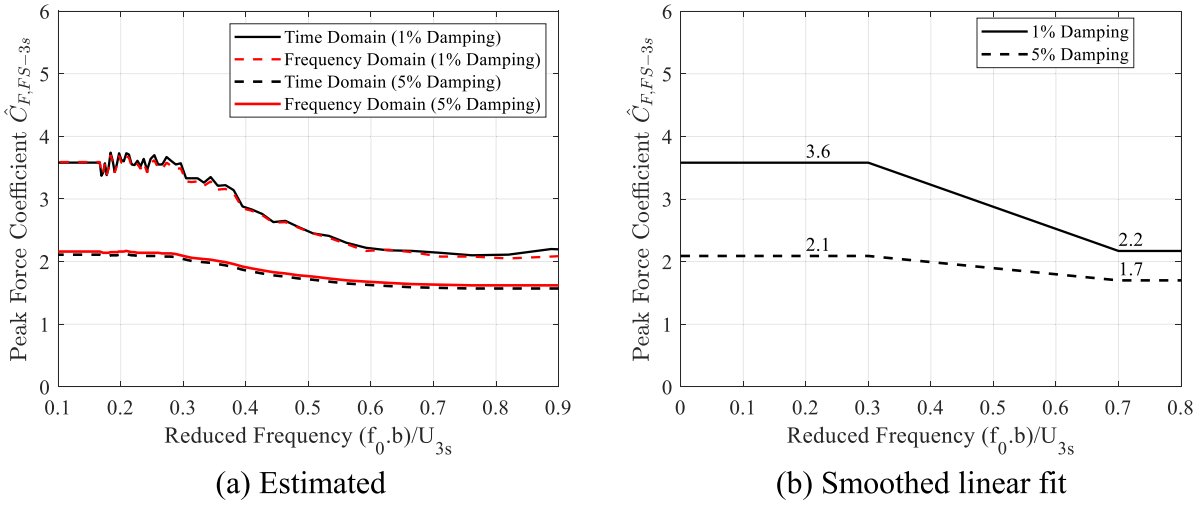

Fig. 11. Peak net force coefficients for test case 3 and 0° tilt angle.

the roof is associated with an increase in the wind loads. For positive tilt angles where the wind is acting towards the PV panels' top surface, positive $\widehat{C}_{F,FS-3s}$ were noticed, and the highest values of about 4 were observed for the 45° PV tilt angle.

4.2. Peak net force coefficients as a function of reduced frequency

The net force coefficient spectra were obtained for various prototype mean wind speeds using $\left|H\left(f_p\right)\right|^2$, as previously described in Section 2 (i.e., Eq. (7)). Essentially, increasing the assumed prototype mean wind speed ($\overline{U}_p$) suggests that the turbulent eddies at full scale are moving faster, causing a shift in the wind turbulence spectrum. This phenomenon was demonstrated in Fig. 10 which shows $\left|H\left(f_p\right)\right|^2$ and the corresponding BLWT net force coefficient spectra for the different $\overline{U}_p$ values. These spectra were used to obtain peak net force coefficients $\widehat{C}_{F,FS-3s}$ using time and frequency domain approaches, as previously described in Section 3.4.

Figs. 11 and 12 show the obtained $\widehat{C}_{F,FS-3s}$ using time and frequency domain approaches for 0° and −45° PV tilt angles, respectively. In addition to the measured damping ratio ζ of 5%, $\widehat{C}_{F,FS-3s}$ were obtained for $\zeta = 1\%$ which also represents a typical in-situ damping ratio of PV panels [19], and the results were presented as a function of the reduced frequency $(f_0.b)/U_{3s}$. It was observed that the time and frequency domain approaches agreed well for the different prototype wind speeds being considered.

In Fig. 11 (test case 3 and 0° tilt angle), three patterns were identified. For $(f_0.b)/U_{3s}$ ranging between 0 and 0.3, it was observed that the estimated $\widehat{C}_{F,FS-3s}$ reached their highest values of 3.6 and 2.1 for 1% and 5% damping, respectively. Then, an approximately linear decrease was detected for $(f_0.b)/U_{3s}$ ranging between 0.3 and 0.7 where $\widehat{C}_{F,FS-3s}$ reached their lowest values of 2.2 and 1.7 for 1% and 5% damping, respectively. The estimated $\widehat{C}_{F,FS-3s}$ remain constant for $(f_0.b)/U_{3s} > 0.7$. It should be noted that the $\widehat{C}_{F,FS-3s}$ values increase with increasing prototype wind speeds, as also reported in Browne et al. [19]. This can be exacerbated by the dynamic resonant effects on PV panels being more pronounced at higher wind speeds.

A similar observation can be made for test case 3 and −45° tilt angle (Fig. 12), where the highest estimated $\widehat{C}_{F,FS-3s}$ are 8.6 and 5.4, and the lowest values are 4.9 and 4.1 for 1% and 5% damping, respectively.

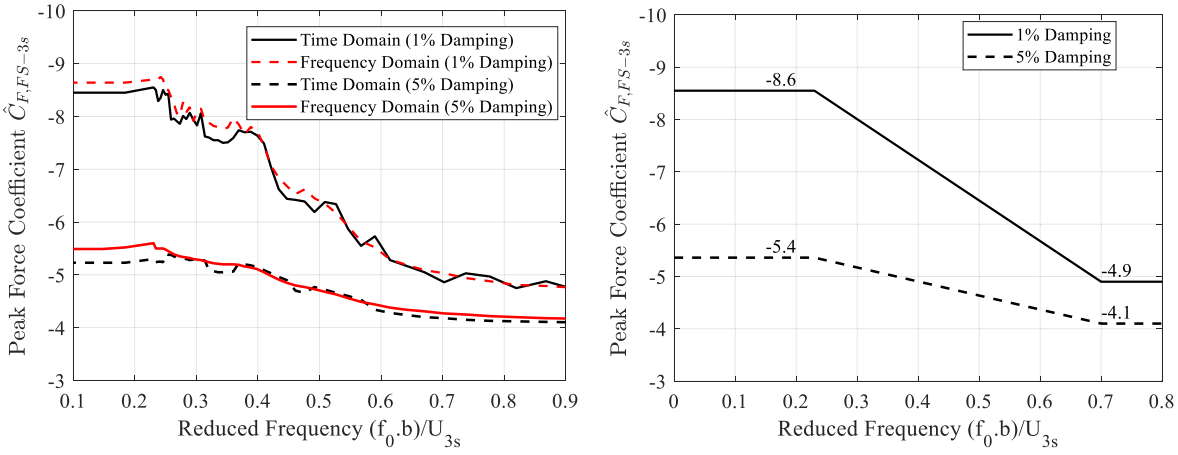

Fig. 12. Peak net force coefficients for test case 3 and −45° tilt angle.

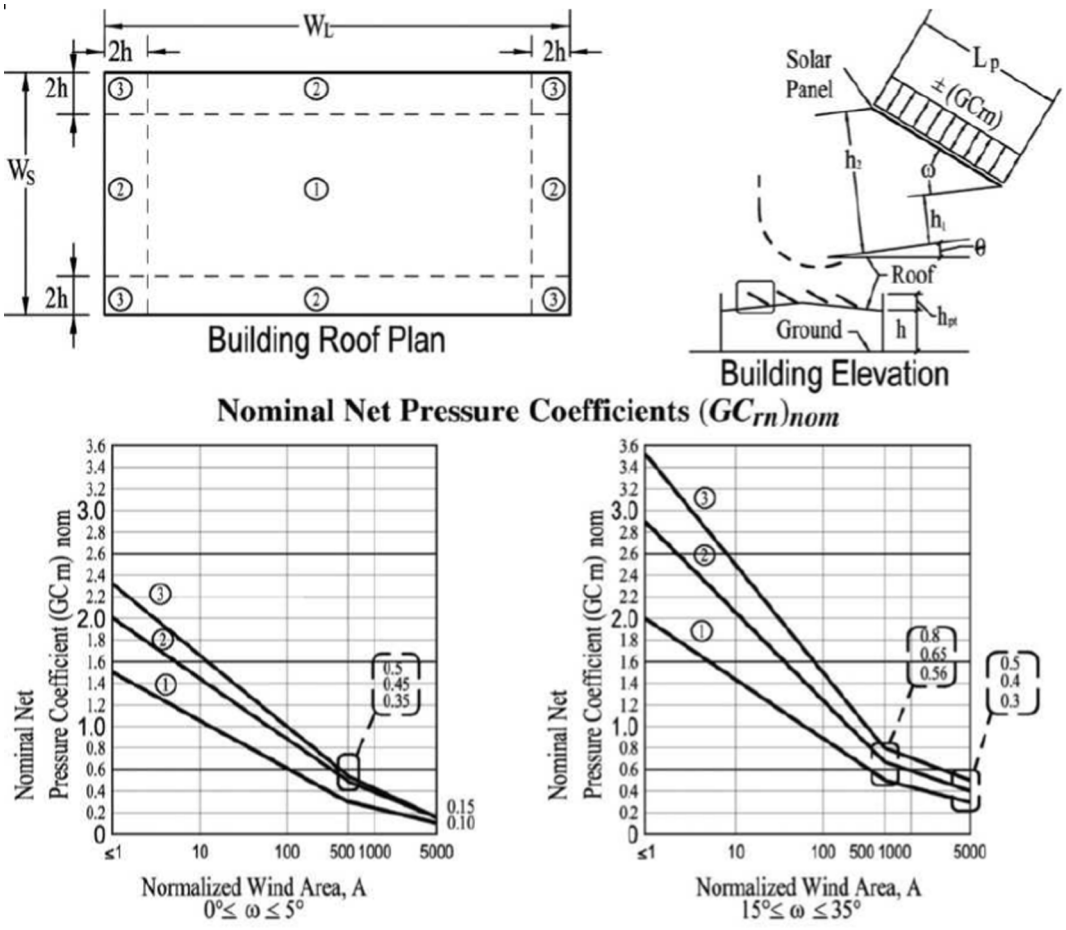

Fig. 13. ASCE 7-16 Fig. 29.4-7 for rooftop solar panels [7].

4.3. Comparison with the ASCE 7-16 Standard

To evaluate the obtained peak net force coefficients $\widehat{C}_{F,FS-3s}$ on the WOW and BLWT rooftop PV panel, a comparison was made with the design pressure coefficients found in ASCE 7-16. The standard provides an equation to calculate the net pressure coefficient GC_{rn}, as shown in Eq. (17). The parapet height factor γ_p and panel chord factor γ_c are defined in Eqs. (18) and (19).

$$(GC_{rn}) = (\gamma_p)(\gamma_c)(\gamma_E)(GC_{rn})_{nom} \tag{17}$$

$$\gamma_p = \min\left(1.2, 0.9 + \frac{h_{pt}}{h}\right) \tag{18}$$

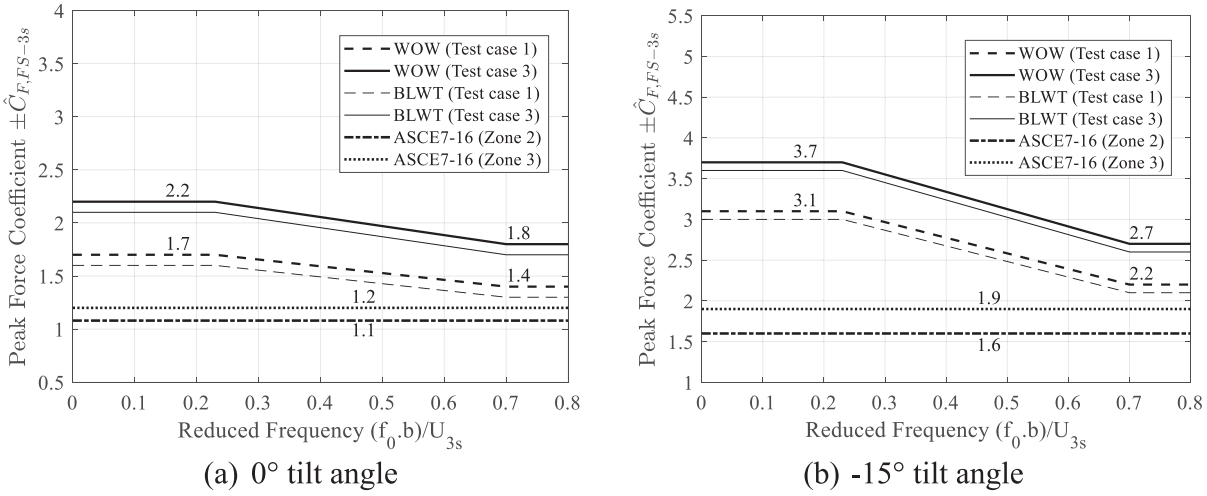

Fig. 14. Comparison of WOW and BLWT $\widehat{C}_{F,FS-3s}$ with GC_{rn} values from ASCE 7-16.

$$\gamma_c = \max\left(0.6 + 0.06L_p, 0.8\right) \tag{19}$$

Fig. 13 shows the building and panel dimensions h_{pt}, h, and L_p, along with the nominal net pressure coefficient $(GC_{rn})_{nom}$ for different roof zones, panel areas, and tilt angles. The parapet height factor is $\gamma_p = 0.9$ and 0.96 for 0° and −15° tilt angles, respectively. The panel chord factor is $\gamma_c = 0.8$, and the array edge factor $\gamma_E = 1.5$ for an "exposed" rooftop PV panel. The normalized wind area A = 70 is a function of the panel area and building dimensions.

WOW and BLWT results of peak force coefficients $\widehat{C}_{F,FS-3s}$ for test cases 1 and 3 and 5% damping ratio were compared with the corresponding GC_{rn} values of ASCE 7-16 for zones 2 and 3, and tilt angles of 0° and −15°. It should be noted that a negative GC_{rn} acts away from the top surface of the PV panel and a positive GC_{rn} acts towards the panel's top surface. The calculated GC_{rn} values for the 0° tilt angle, were found to be 1.1 and 1.2 for ASCE 7-16 zones 2 and 3, respectively. For a tilt angle of −15°, GC_{rn} values were found to be 1.6 and 1.9 for ASCE 7-16 zones 2 and 3, respectively.

Fig. 14 shows a comparison of the estimated $\widehat{C}_{F,FS-3s}$ values on the WOW and BLWT models, including dynamic resonant effects for 5% damping, with the GC_{rn} values from ASCE 7-16. Wind-induced dynamic effects on rooftop PV panels are not accounted for in the ASCE 7-16 Standard. This justifies the reason behind GC_{rn} values being constant for the whole range of wind speeds. It is evident in Fig. 14 that the GC_{rn} values were lower than $\widehat{C}_{F,FS-3s}$ for all considered cases and reduced frequency values with differences ranging between 20% and 48%. Hence, the ASCE 7-16 Standard underestimates the peak net pressure coefficients that are missing dynamic effects.

5. Conclusion

A new experimental-numerical approach is proposed in this study to estimate the peak wind loads on PV systems by incorporating the effects of inflow turbulence and resonance. Net uplift force coefficient data on a rooftop PV panel, obtained from full-scale system-level tests (at the WOW) and rigid scale model tests (at a BLWT), were used to demonstrate the proposed method. Also, a simplified spectral approach was adopted to calculate the peak force coefficients as functions of reduced frequency. A reasonable agreement was observed between the compensated peak net force coefficients using the time and frequency domain approaches. Also, a comparison was made between the estimated WOW and BLWT peak force coefficients, including dynamic effects, with those found in ASCE 7-16. It was observed that the Standard underestimates the peak net pressure coefficients, mainly because the dynamic effects were not accounted for. Validation of the proposed approach is underway using data from field measurements on rooftop PV systems at CWU. The field measurements will be compared to those obtained from a full-scale PV array at the NSF NHERI WOW EF at FIU. The effect of aerodynamic damping will be also assessed as a function of wind speed. Such study is expected to advance knowledge on smaller structures such as PV arrays that are sensitive to wind-induced dynamic effects.

CRediT authorship contribution statement

Johnny Estephan: Conceptualization, Formal analysis, Methodology, Writing – original draft, Writing – review & editing. **Arindam Gan Chowdhury:** Conceptualization, Supervision, Resources, Funding acquisition, Writing – review & editing. **Peter Irwin:** Conceptualization, Supervision, Validation, Writing – review & editing.

Declaration of Competing Interest

The authors declare that they have no known competing financial interests or personal relationships that could have appeared to influence the work reported in this paper.

Acknowledgments

The authors would like to acknowledge the National Science Foundation (NSF) support for a collaborative project (Award No. 1825908) and the Natural Hazards Engineering Research Infrastructure (NHERI) award (NSF Award No. 1520853 and 2037899) to the WOW EF. The contributions of Dr. Mohammadtaghi Moravej (Walker Consultants, Los Angeles, CA, USA) and Dr. Emil Simiu in terms of supporting this work are greatly acknowledged. The authors would also like to acknowledge the help of the WOW EF and RWDI BLWT teams of researchers and engineers in conducting the experiments. The views and opinions expressed in this paper are those of the authors and do not necessarily reflect the position of the funding agencies.

References

[1] Solar Energy Industries Association. U S Surpasses 2 Million Sol Install; 2019. www.seia.org (accessed October 30, 2021).
[2] Andolsek E. Study of full-scale rooftop solar panels subject to wind loads. University of Colorado Denver; 2013.
[3] Harris JD. Study of wind loads applied to rooftop solar panels. University of Colorado Denver; 2013.
[4] Plas R. Study of wind loads applied to solar panels on flat rooftops. University of Colorado Denver; 2015.

[5] Bender W, Waytuck D, Wang S, Reed DA. In situ measurement of wind pressure loadings on pedestal style rooftop photovoltaic panels. Eng Struct 2018;163:281–93. https://doi.org/10.1016/j.engstruct.2018.02.021.
[6] Reed D, Morrison M, Bender W, Wang S. Measurement and analysis of wind loadings on rooftop photovoltaic panels, Miami, Florida: 2016.
[7] ASCE 7. Minimum Design Loads and Associated Criteria for Buildings and Other Structures. Reston, VA: Reston, VA: ASCE/SEI 7–16; 2016.
[8] Banks D. The role of corner vortices in dictating peak wind loads on tilted flat solar panels mounted on large, flat roofs. J Wind Eng Ind Aerodyn 2013;123:192–201. https://doi.org/10.1016/j.jweia.2013.08.015.
[9] Browne MTL, Gibbons MPM, Gamble S, Galsworthy J. Wind loading on tilted rooftop solar arrays: the parapet effect. J Wind Eng Ind Aerodyn 2013;123:202–13. https://doi.org/10.1016/j.jweia.2013.08.013.
[10] Cao J, Yoshida A, Saha PK, Tamura Y. Wind loading characteristics of solar arrays mounted on flat roofs. J Wind Eng Ind Aerodyn 2013;123:214–25. https://doi.org/10.1016/j.jweia.2013.08.014.
[11] Erwin J, Bitsuamlak G, Chowdhury AG, Barkaszi S, Gamble S. Full Scale and Wind Tunnel Testing of a Photovoltaic Panel Mounted on Residential Roofs. Adv. Hurric. Eng., Miami, Florida, United States: American Society of Civil Engineers; 2012, p. 471–82. DOI: 10.1061/9780784412626.041.
[12] Kopp GA, Surry D, Chen K. Wind loads on a solar array. Wind Struct 2002;5:393–406. https://doi.org/10.12989/WAS.2002.5.5.393.
[13] Kopp GA. Wind loads on low-profile, tilted, solar arrays placed on large, flat. Low-Rise Building Roofs J Struct Eng 2013;140:04013057. https://doi.org/10.1061/(ASCE)ST.1943-541X.0000825.
[14] Kopp GA, Farquhar S, Morrison MJ. Aerodynamic mechanisms for wind loads on tilted, roof-mounted, solar arrays. J Wind Eng Ind Aerodyn 2012;111:40–52. https://doi.org/10.1016/j.jweia.2012.08.004.
[15] Meroney RN, Neff DE. Wind effects on roof-mounted solar photovoltaic arrays: CFD and wind-tunnel evaluation. Fifth Int. Symp. Comput. Wind Eng. CWE2010, Chapel Hill, North Carolina, USA: 2010.
[16] Stathopoulos T, Zisis I, Xypnitou E. Local and overall wind pressure and force coefficients for solar panels. J Wind Eng Ind Aerodyn 2014;125:195–206. https://doi.org/10.1016/j.jweia.2013.12.007.
[17] Wood GS, Denoon RO, Kwok KCS. Wind loads on industrial solar panel arrays and supporting roof structure. Wind Struct 2001;4:481–94. https://doi.org/10.12989/WAS.2001.4.6.481.
[18] Naeiji A, Raji F, Zisis I. Wind loads on residential scale rooftop photovoltaic panels. J Wind Eng Ind Aerodyn 2017;168:228–46. DOI: 10.1016/j.jweia.2017.06.006.
[19] Browne MTL, Taylor ZJ, Li S, Gamble S. A wind load design method for ground-mounted multi-row solar arrays based on a compilation of wind tunnel experiments. J Wind Eng Ind Aerodyn 2020;205:104294. https://doi.org/10.1016/j.jweia.2020.104294.
[20] Moravej M, Chowdhury A, Irwin P, Zisis I. Dynamic effects of wind loading on photovoltaic systems. Proc. 14th Int. Conf. Wind Eng., Porto Alegre, Brazil: 2015.
[21] Moravej M. Investigating scale effects on analytical methods of predicting peak wind loads on buildings. FIU Electron Theses Diss 2018. https://doi.org/10.25148/etd.FIDC006834.
[22] Chowdhury AG, Zisis I, Irwin P, Bitsuamlak G, Pinelli J-P, Hajra B, et al. Large-Scale Experimentation Using the 12-Fan Wall of Wind to Assess and Mitigate Hurricane Wind and Rain Impacts on Buildings and Infrastructure Systems. J Struct Eng 2017;143. DOI: 04017053.
[23] Estephan Johnny, Gan Chowdhury Arindam, Elawady Amal, Erwin James. Dependence of internal pressure in low-rise buildings on aerodynamic parameters, defect features and background leakage. J Wind Eng Ind Aerodyn 2021;219:104822. https://doi.org/10.1016/j.jweia.2021.104822.
[24] Mooneghi MA, Irwin P, Chowdhury AG. Partial turbulence simulation method for predicting peak wind loads on small structures and building appurtenances. J Wind Eng Ind Aerodyn 2016;157:47–62. DOI: 10.1016/j.jweia.2016.08.003.
[25] Chowdhury AG, Vutukuru KS, Moravej M. Full- and Large-Scale Experimentation Using the Wall of Wind to Mitigate Wind Loading and Rain Impacts on Buildings and Infrastructure Systems. Proc. Struct. Eng. Conv., Jadavpur University, India: 2018.
[26] Banks D, Guha TK, Fewless YJ. A hybrid method of generating realistic full-scale time series of wind loads from large-scale wind tunnel studies: Application to solar arrays. Proc. 14th Int. Conf. Wind Eng., Porto Alegre, Brazil: 2015.
[27] Guo Y, Wu C-H, Kopp GA. A method to estimate peak pressures on low-rise building models based on quasi-steady theory and partial turbulence analysis. J Wind Eng Ind Aerodyn 2021;218:104785. https://doi.org/10.1016/j.jweia.2021.104785.
[28] Naeiji A. Wind Loads on Residential Rooftop Solar Photovoltaic Panels. FIU Electronic Theses and Dissertations. Florida International University, 2017. DOI: 10.25148/etd.FIDC006588.
[29] Braun R, Chen D, Chowdhury A, Estephan J, Gordon C, Irwin P, et al. Peak Wind Effects on Low-Rise Building Roofs and Rooftop PV Arrays. 6th Am. Assoc. Wind Eng. Workshop, Clemson, SC, USA: 2021, p. 4.
[30] Vutukuru KS, Alawode K, Bakhtiari A, Elawady A, Lee SJ, Gan Chowdhury A, et al. Full-Scale Experimental Testing to Investigate Wind-Induced Vibrations on Curtain Wall Systems. Proc. Int. Struct. Eng. Constr., vol. 8, 2021. DOI: 10.14455/ISEC.2021.8(1).STR-12.
[31] Miller R, Zimmerman D. Wind loads on flat plate photovoltaic array fields. Seattle, Washington: Boeing Engineering and Construction Company; 1979.
[32] SEAOC P.V.2. Wind Design for Solar Arrays. Structural Engineers Association of California; 2017.
[33] Holmes JD, Bekele S. Wind Loading of Structures. 4th ed. Boca Raton: CRC Press; 2021.
[34] Irwin P, Cooper KR, Girard R. Correction of distortion effects caused by tubing systems in measurements of fluctuating pressures. J Wind Eng Ind Aerodyn 1979;5:93–107. https://doi.org/10.1016/0167-6105(79)90026-6.
[35] ESDU. Characteristics of the Atmospheric Boundary Layer, Part II: Single Point Data for Strong Winds (Neutral Atmosphere). London: Engineering Sciences Data Unit; 2001.
[36] Richards PJ, Hoxey RP. Pressures on a cubic building—Part 1: Full-scale results. J Wind Eng Ind Aerodyn 2012;102:72–86. https://doi.org/10.1016/j.jweia.2011.11.004.
[37] Levitan ML, Mehta KC. Texas Tech field experiments for wind loads part 1: building and pressure measuring system. J Wind Eng Ind Aerodyn 1992;43:1565–76. https://doi.org/10.1016/0167-6105(92)90372-H.
[38] Levitan ML, Mehta KC. Texas tech field experiments for wind loads part II: meteorological instrumentation and terrain parameters. J Wind Eng Ind Aerodyn 1992;43:1577–88. https://doi.org/10.1016/0167-6105(92)90373-I.
[39] Jeary AP. Establishing non-linear damping characteristics of structures from non-stationary response time-histories. Struct Eng 1992;70:61–6.
[40] Tamura Y, Suganuma S. Evaluation of amplitude-dependent damping and natural frequency of buildings during strong winds. J Wind Eng Ind Aerodyn 1996;59:115–30. https://doi.org/10.1016/0167-6105(96)00003-7.
[41] Brigham EO, Morrow RE. The fast Fourier transform. IEEE Spectr 1967;4:63–70. https://doi.org/10.1109/MSPEC.1967.5217220.
[42] Lieblein J. Efficient methods of extreme-value methodology. Gaithersburg, MD: National Bureau of Standards; 1974. DOI: 10.6028/NBS.IR.74-602.
[43] Estephan J, Feng C, Gan Chowdhury A, Chavez M, Baskaran A, Moravej M. Characterization of wind-induced pressure on membrane roofs based on full-scale wind tunnel testing. Eng Struct 2021;235. https://doi.org/10.1016/j.engstruct.2021.112101.